Electronic Supplementary Material (ESI) for Nanoscale.

Confinement of Single Polyoxometalate Clusters in Molecular-Scale Cages for Improved Flexible Solid-State Supercapacitors

Meiling Wang[a,c,1], Yong Zhang[c,1], Tianyuan Zhang[d], Yue Li[a], Mingzhu Cui[e], Xun Cao[c], Yu Lu[c], Dongdong Peng[c], Weifeng Liu[a], Xuguang Liu[a]*, Tian Wang*[b], Yizhong Huang[c]

[a] *Institute of New Carbon Materials, Taiyuan University of Technology, Taiyuan 030024, Shanxi, China*

[b] *Department of Chemistry, National University of Singapore, 3 Science Drive 3, 117543, Singapore*

[c] *School of Materials Science and Engineering, Nanyang Technological University, 50 Nanyang Avenue, 639798, Singapore*

[d] *Department of Chemistry, University of Washington, Seattle, Washington 98195, United States*

[e] *Institute of Crystalline Materials, Shanxi University, Taiyuan, Shanxi 030006, China*

* Corresponding author. Email: liuxuguang@tyut.edu.cn *; tian.wang91@u.nus.edu; * yzhuang@ntu.edu.sg

[1] Contributed equally to this work.

Electrochemical Measurement

Fabrication of Electrodes in a Traditional Three-Electrode System

All electrochemical tests were performed in an electrochemical workstation (CHI 760E). In the three electrode tests, PMo_{12}/PPy/CNT hydrogel dispersion without binder was directly coated on carbon paper (working area 0.25 cm^2), after drying under an infrared lamp, it was used as working electrode. As shown in Figure S9, PMo_{12}/PPy/CNT ternary hybrid hydrogel can be well dispersed in water, so during the electrode preparation process, no additional binder is required during the coating process, while traditional composite materials require the addition of PVDF as a binder, which is not conductive. And an Ag/AgCl electrode (saturated by 3 M KCl), and a piece of Pt sheet electrode were used as reference and counter electrodes, respectively. Finally, 0.5 M H_2SO_4 or 1 M [Bmim]HSO_4 aqueous solution were compared as the electrolyte in the electrochemical measurement.

Fabrication of Aqueous Supercapacitor

Before the two-electrode test, PMo_{12}/PPy/CNT ternary composite hydrogel dispersion (250 μL, 10 mg/mL) was evenly coated on carbon paper or carbon cloth (working area 1 cm^2) and dried under infrared lamp. In the liquid-state test, two pieces of as-prepared electrodes (1cm × 2 cm) were pressed together with a wet filter soaked with 1 M [Bmim]HSO_4 as electrolyte and separator.

Fabrication of Flexible-Solid-State Supercapacitor

In the two-electrode solid-state test, the wet-separator was replaced with solid PVA/[Bmim]HSO_4 gel electrolyte, which was prepared as follows: 2.36 g of [Bmim]HSO_4 was added into 10 mL of deionized water, and then 1 g of PVA power

was added. The mixture was heated to 95°C under stirring until the solution became clear. The hot PVA/[Bmim]HSO_4 gel electrolyte was evenly dropped onto two pieces of as-prepared electrodes with carbon paper or carbon cloth as collector and then pressed together. After the electrolyte cooled and became hard, the thickness of the device was around 0.5 mm for solid-state device with carbon paper as collector and 1 mm for flexible SSC with carbon cloth as collector. Electrochemical impedance spectroscopy (EIS) measurements of PMo_{12}/PPy/CNT-SSC and PMo_{12}/PPy/CNT hybrid hydrogel-SSC were conducted at amplitude of 5 mV over a frequency range of 0.01 Hz-100 kHz.

To avoid the evaporation of electrolyte, both the LSC and ASC were encapsulated with flexible plastic film. Experiments show that although carbon paper cannot be bent, the SSC constructed with carbon paper as collector has the similar performance as that with carbon cloth as current collector.

CV and GCD measurements were performed at potential ranging from -0.2 to 0.8 V for the three-electrode system. And CV measurements were performed from -0.4 to 0.8 V while GCD measurements from 0 to 0.8 V for the two-electrode liquid-state system. In the two-electrode solid-state system, various voltage ranges (0-1.2 V, 0-1.4 V and 0-1.6 V) were measured for CV and GCD. EIS measurement was conducted for the two-electrode flexible-solid-state system over a frequency range of 100 kHz to 0.01 Hz.

Electrochemical Performance Evaluation

As for the three-electrode system, the specific capacitance (C_m) of

PMo_{12}/PPy/CNT gel-based electrodes was evaluated by the following equations $C_m = \frac{\int IdV}{m\vartheta\Delta V}$ (for CV) and $C_m = \frac{I\Delta t}{m\Delta V}$ (for GCD), where ∫IdV is the integrating area of CV curves, m is the mass of active materials, ϑ is scan rate, ΔV is the potential window after IR drop, I is discharge current, and Δt is discharge time.

The specific capacitance (C_m) and areal capacitance (C_a) of the two-electrode systems were calculated according to the following equations $C_m = \frac{\int IdV}{m\vartheta\Delta V}$ and $C_a = \frac{\int IdV}{A\vartheta\Delta V}$ (for CV), and $C_m = 2\frac{I\Delta t}{m\Delta V}$ and $C_a = 2\frac{I\Delta t}{A\Delta V}$ (for GCD), where ∫IdV, ϑ, ΔV and I represent same meaning as above. In this case, m is the mass of active material in single electrode; A is the active area of single electrode.

The energy density (E, μWh cm^{-2}) and power (P, μW cm^{-2}) of SSCs were determined from GCD curves using the equations $E = \frac{1}{2} \times \frac{1}{3600} C_a \cdot \Delta V^2$ and $P = \frac{3600 \times E}{\Delta t}$.

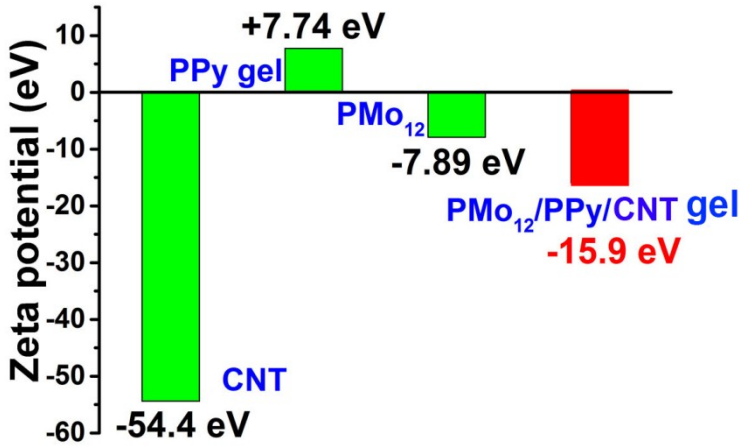

Figure S1. Zeta potential of CNT, PPy hydrogel, PMo_{12} and PMo_{12}/PPy/CNT hybrid hydrogel

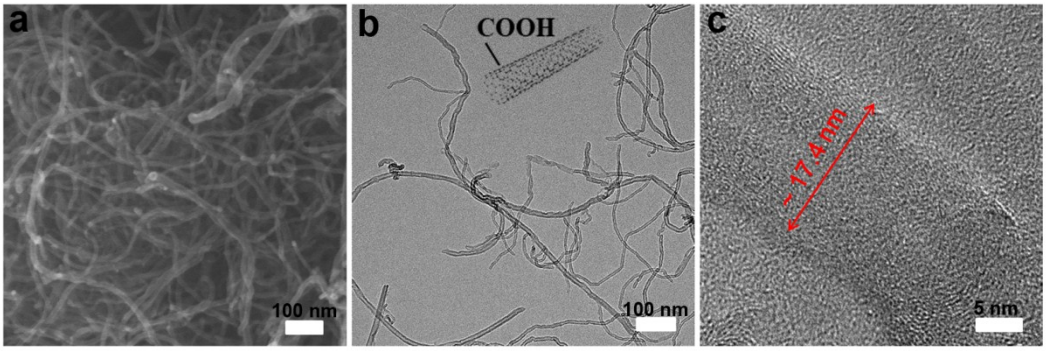

Figure S2. SEM (a), TEM (b) and HRTEM images of acidified CNT (c)

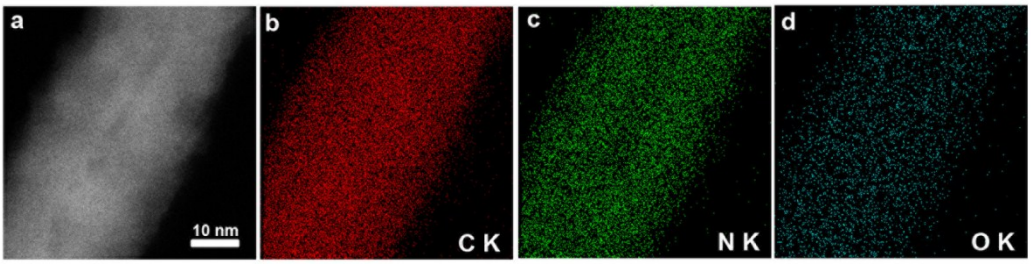

Figure S3. STEM-EDS elemental mapping of PPy/CNT hybrid hydrogel

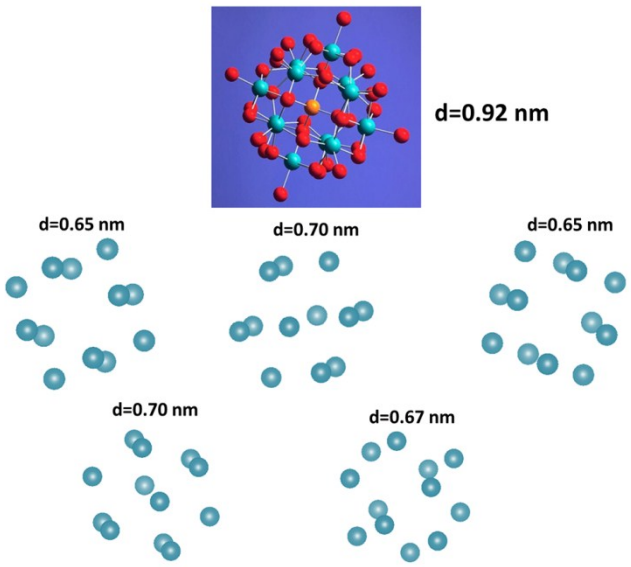

Figure S4. (a) Molecular structure of Keggin $[PMo_{12}O_{40}]^{3-}$ cluster, (b) $PMo_{12}O_{40}$ cluster with random orientations (only Mo atoms are visible) deposited on PPy hydrgoel wrapped CNT. Blue=Mo, Red=O, Yellow=P.

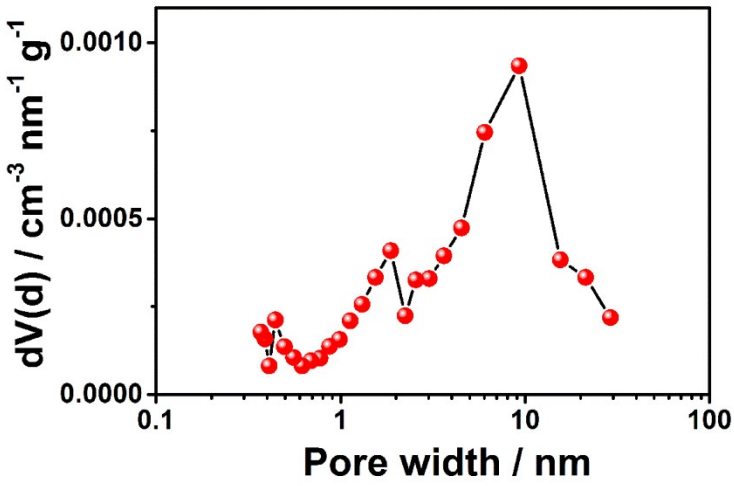

Figure S5. The pore-size distribution plot for hybrid hydrogel sample.

Table S1. XPS analysis results of Mo_{3d} spectra obtained from PMo_{12}/PPy/FCNT hybrid hydrogel and PMo_{12}/PPy/FCNT composite

Binding energy (eV)	Oxidation state		Area %	
			PMo_{12}/PPy/FCNT hydrogel	PMo_{12}/PPy/FCNT composite
231.9	Mo $3d_{5/2}$	5+	9.0	7.9
233		6+	50.9	52.0
235	Mo $3d_{3/2}$	5+	6.0	5.3
236.1		6+	33.9	34.7
	FWHM (eV)		1.5 eV	1.4 eV

FWHM, full-width at half-maximum

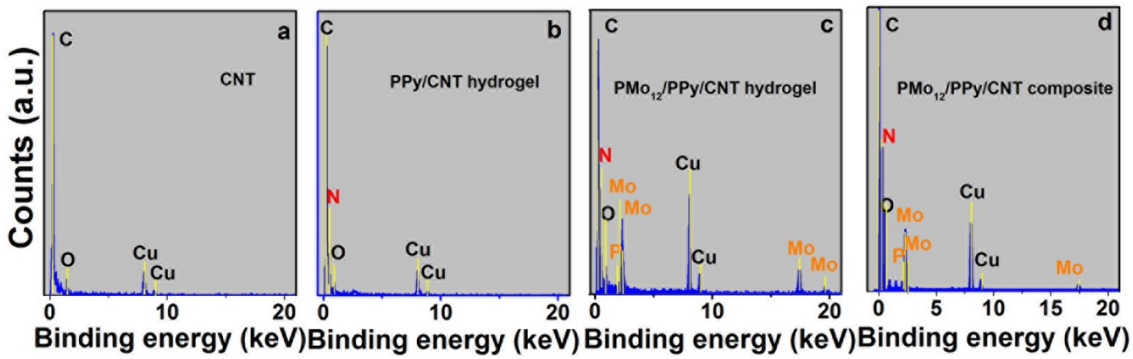

Figure S6. Energy dispersive X-ray spectrometry (EDX) spectrum of acidified CNT (a), PPy/CNT hybrid hydrogel (b) and PMo_{12}/PPy/CNT hybrid hydrogel (c) and PMo_{12}/PPy/CNT composite (d)

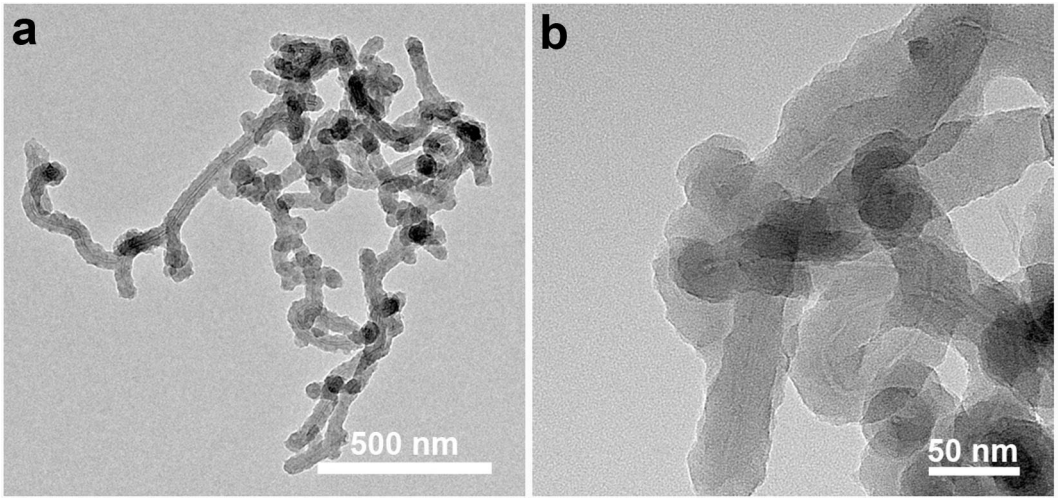

Figrue S7. TEM images of PPy/CNT hydrid hydrogel at different magnifacition

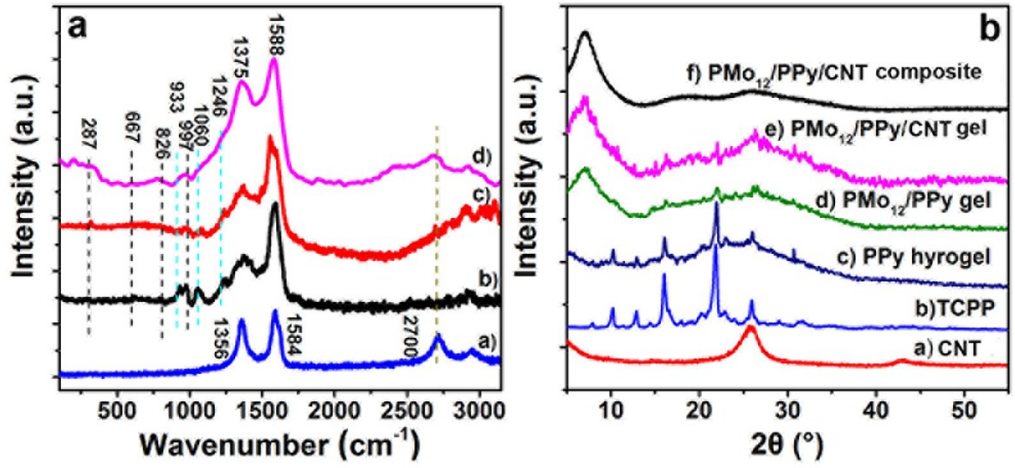

Figure S8. (a) Raman spectra of a) CNT, b) PMo_{12}/PPy gel, c) PMo_{12}/PPy/CNT hybrid hydrogel and d) PMo_{12}/PPy/CNT hybrids; (b) XRD patterns of a) CNT b) TCPP, c) PPy hydrogel, d) PMo_{12}/PPy hybrid hydrogel, e) PMo_{12}/PPy/CNT hybrid hydrogel and f) PMo_{12}/PPy/CNT composite

The structures of PMo_{12}/PPy/CNT hybrid hydrogel were characterized by Raman spectra (Figure S8a). The D and G bands and the overtone of D band were observed at 1,356, 1,584 and 2,700 cm^{-1}, respectively, in the spectrum of CNT (curve a). In the spectrum of PMo_{12}/PPy hybrid hydrogel (curve b), the bands at 1375 and 1588 cm^{-1} are ascribed to C=C stretching modes of PPy. Meanwhile, a series of characteristic Raman bands for PPy centered at about 933, 1060, 1246 cm^{-1} assigning to C-H out-of-plane deformation, ring deformation and C-H in-plane deformation, respectively, all indicate the successful polymerization of Py. And the TEM image of PMo_{12}/PPy hybrid hydrogel (Figure S8) also shows same porous structure as the PPy hydrogel (Figure S9). The two bands at 1375 and 1588 cm^{-1} also appear in the spectra of PMo_{12}/PPy/CNT ternary hybrid hydrogel (curve c) and PMo_{12}/PPy/CNT composite (curve d). However, there are nearly no distinct Raman peaks apart from a weak band at 2700 cm^{-1} originating from CNT, implying that the surfaces of CNT in both hybrids are covered. In addition, it can be seen that the four main peaks presented at 997, 826, 667 and 287 cm^{-1} are similar in samples arising from loaded PMo_{12} (curve b-d), evidencing the structure of PMo_{12} integrated into these hybrid materials[1] is preserved during and after the assembly process. This region was totally silent for pristine CNTs.

Figure S8b compares the XRD patterns for different samples. Two hump diffraction peaks at ~26° and ~44° in curve a can be ascribed to the typical graphite-like structure (002) and (100) of CNT, respectively. Curve c shows a broad peak between 20° and 30°, which is consistent with pure PPy, revealing its amorphous nature of PPy hydrogel. It also exhibits some weak characteristic peaks of TCPP

cross-linker as presented in curve b, indicating the doping of TCPP. In contrast to pure PPy hydrogel, PMo_{12}/PPy hydrogel (curve d), PMo_{12}/PPy/CNT hydrogel (curve e) and PMo_{12}/PPy/CNT composite (curve f) all exhibit a new and sharp diffraction peak at 6.7° from PMo_{12}[2]. After modification, the characteristic peaks of CNT in PMo_{12}/PPy/CNT hybrid hydrogel and conventional composite become weaker, which is in agreement with Raman results. Also, it should be noted that the characteristic peaks of TCPP are not observed in conventional composite.

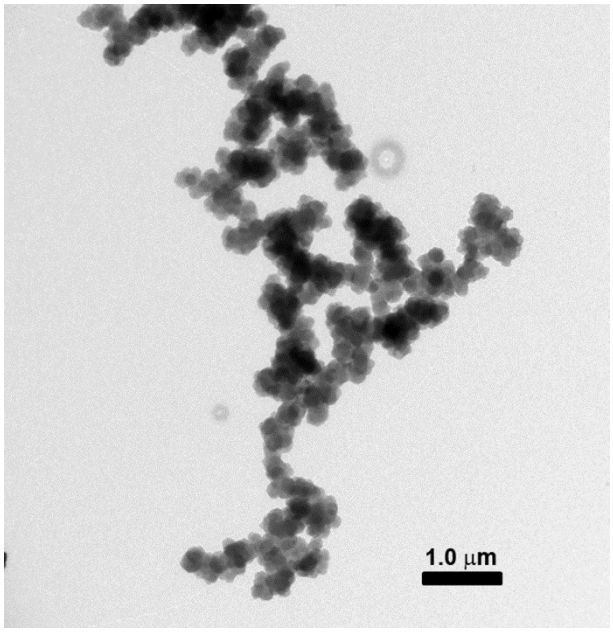

Figure S9. TEM image of pure PPy hydrogel

Figure S10. Digital photos of PMo_{12}/PPy/CNT hybrid hydrogel (a and a') and conventional PMo_{12}/PPy/CNT composite (b and b') after ultrasounding in water for 30 min (a and b) and continue standing for 6 h (a' and b')

PMo_{12}/PPy/CNT ternary hybrid hydrogel can be well dispersed, which has been demonstrated by no precipitation in water even after standing for 6 h, indicating its higher hydrophilicity of the hybrid hydrogel. Because of this, we have created a more uniform coating during the electrode preparation process, and no additional binder is required during the coating process, while traditional composite materials also require the addition of PVDF as a binder, which is not conductive. Not only will it cover the active site, but it will also block proton and electron transport. This preparation method simplifies the preparation process, and also eliminates substances that may block and transport electrons, thereby increasing conductivity.

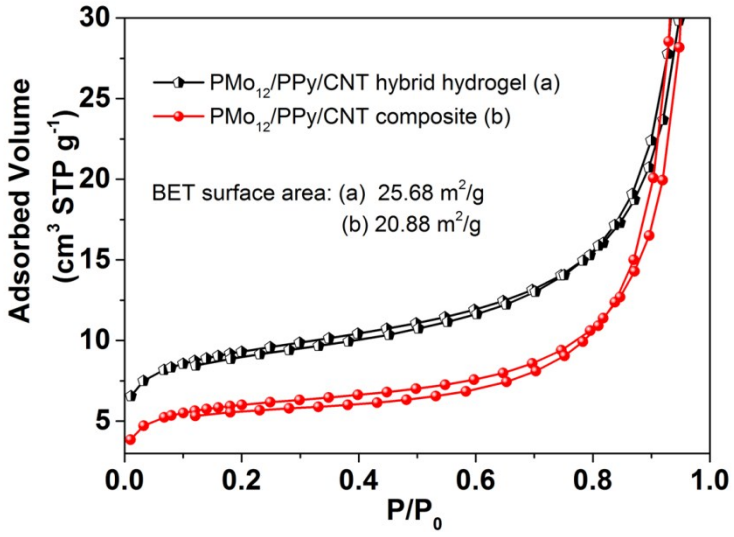

Figure S11. Nitrogen sorption isotherm of hybrid hydrogel and conventional composite

The N_2 adsorption-desorption isotherm plots show that the Brunauer-Emmett-Teller (BET) specific surface area of PMo_{12}/PPy/CNT ternary hybrid hydrogel is higher than that of conventional composite when the loading amount of PMo_{12} is the same. The fishnet-like PPy hydrogel may make contribution.

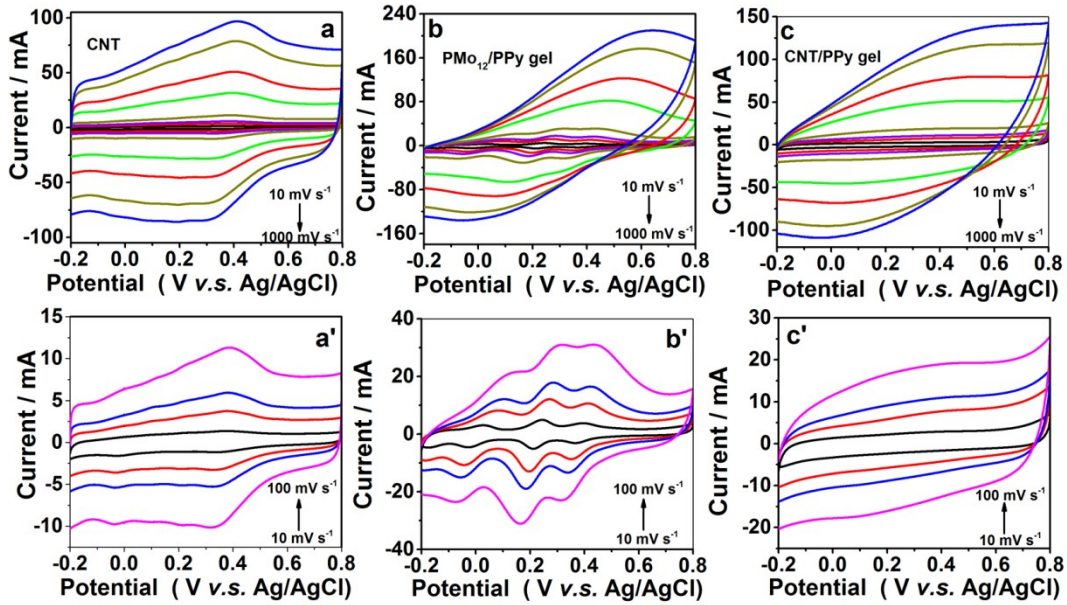

Figure S12. CV curves of CNT (a, a'), PMo_{12}/PPy gel (b, b') and PPt/CNT gel (c, c') at scan rates of 10, 30, 50, 100, 300, 500, 800, 1000 mV/s in 0.5 M H_2SO_4 solution

A wide reversible hump is observed in Figure S12A, suggesting a large faradaic contribution to the overall performance due to the doping of O^3. The regular shape keeps unchanged obviously with the increase of scan rate even to 1000 mV s^{-1}, implying a fast charge/discharge process[4]. However, it is found that for both PMo_{12}/PPy gel (Figure S12b, b') and PPy/CNT gel (Figure S12c, c'), good capacitance behavior occurs in range from 10 to100 mV s^{-1} and the waves are unevenly shaped with the further increase of scan rate.

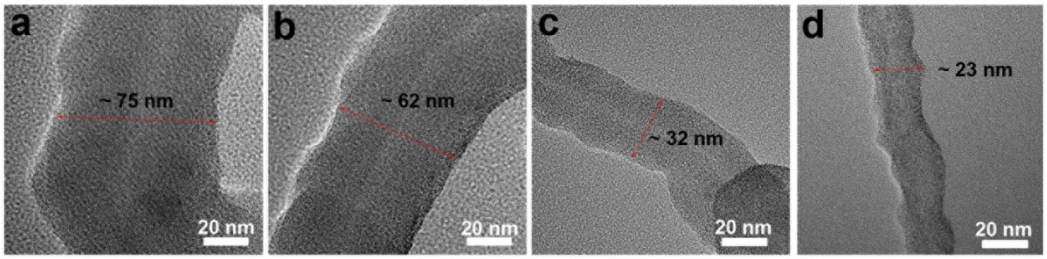

Figure S13. TEM images of (a) $PMo_{12}/PPy/CNT_5$ gel, (b) $PMo_{12}/PPy/CNT_{10}$ gel, (c) $PMo_{12}/PPy/CNT_{15}$ gel and (d) $PMo_{12}/PPy/CNT_{20}$ gel

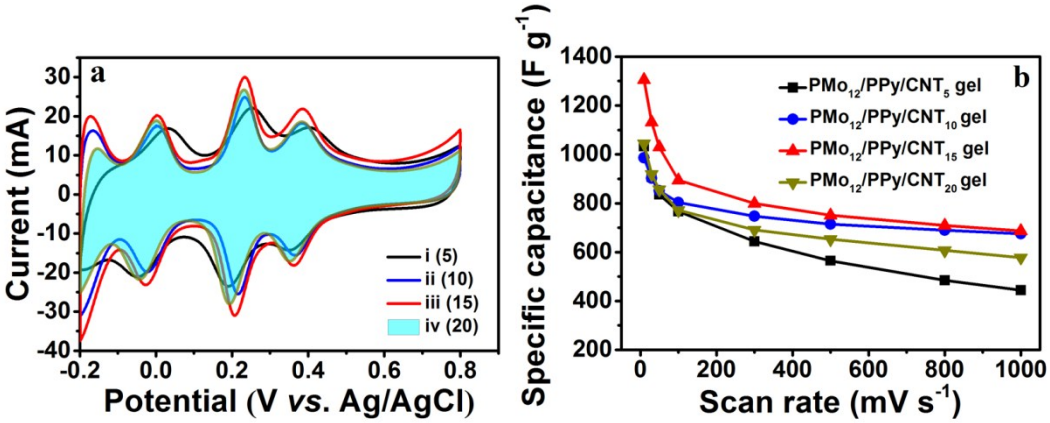

Figure S14. (a) CV curves of $PMo_{12}/PPy/CNT$ ternary hybrid hydrogel with different amounts of CNT: (i) $PMo_{12}/PPy/CNT_5$ gel, (ii) $PMo_{12}/PPy/CNT_{10}$ gel, (iii) $PMo_{12}/PPy/CNT_{15}$ gel and (iv) $PMo_{12}/PPy/CNT_{20}$ gel at 50 mV s^{-1}; the plots of related specific capacitances versus scan rate

Figure S12 shows the TEM images of $PMo_{12}/PPy/CNT_5$ gel, $PMo_{12}/PPy/CNT_{10}$ gel, $PMo_{12}/PPy/CNT_{15}$ gel and $PMo_{12}/PPy/CNT_{20}$ gel, which are named according to the amount of CNT introduced. It can be found that the more the amount of CNT, the thinner the coated PPy hydrogel. Figure S13 depicts the influence of CNT on the

specific capacitance of ternary hybrid hydrogel. It can be seen from the Figure S13a that all the CVs of ternary hybrid hydrogels doped with different amounts of CNT reveal three characteristic redox peaks and the redox current of three peaks increases with the incensement of the mass content of CNT from 5 to 15 wt%, indicating an improved enhancement effect for that the addition of CNT can increase the conductivity, but too much CNT pulls down the total capacitance as a result of its relatively low intrinsic capacitance. Based on the CV curves at different scan rates, the specific capacitance of ternary hybrid hydrogels doped with different amount of CNT is calculated. The related plots of specific capacitance versus scan rate are shown in Figure S13b. $PMo_{12}/PPy/CNT_{15}$ gel shows highest capacitance performance. So the optimized $PMo_{12}/PPy/CNT_{15}$ gel is chosen in our study.

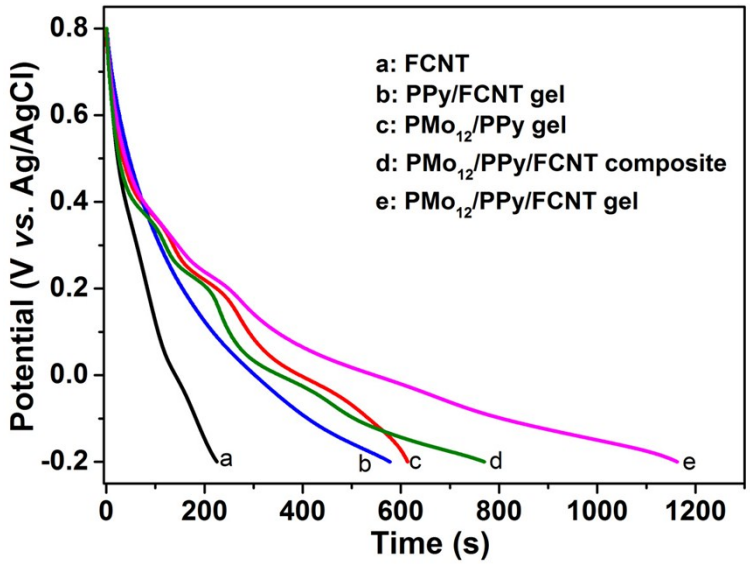

FiguRe S15. GCD curves of these active materials at current density of 1 A g^{-1}

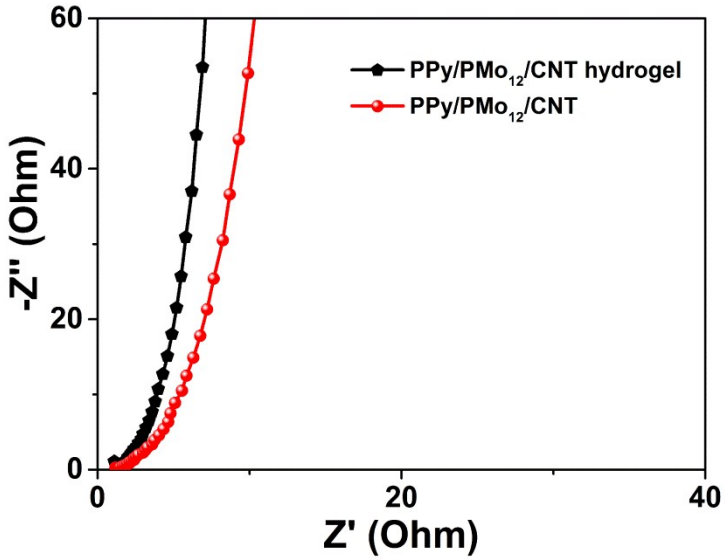

Figure S16. EIS diagram of hybrid hydrogel and conventional composite in three electrode system

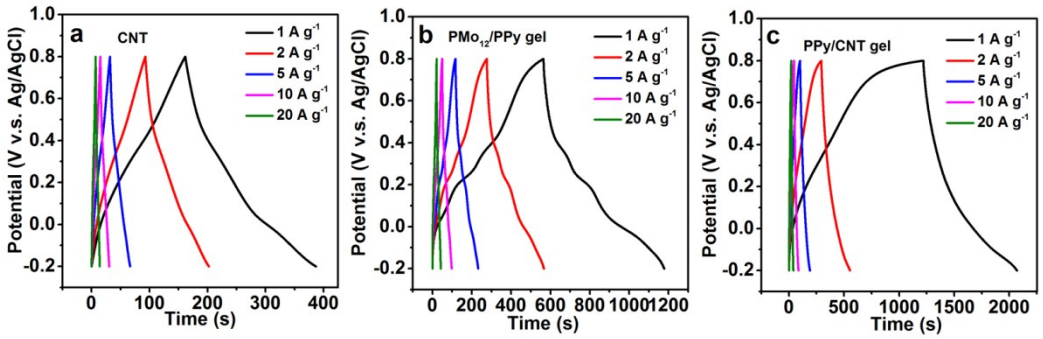

Figure S17. Galvanostatic charge-discharge curves CNT (a), PMo_{12}/PPy gel (b) and PPy/CNT gel (c) in 0 .5 M H_2SO_4 solution

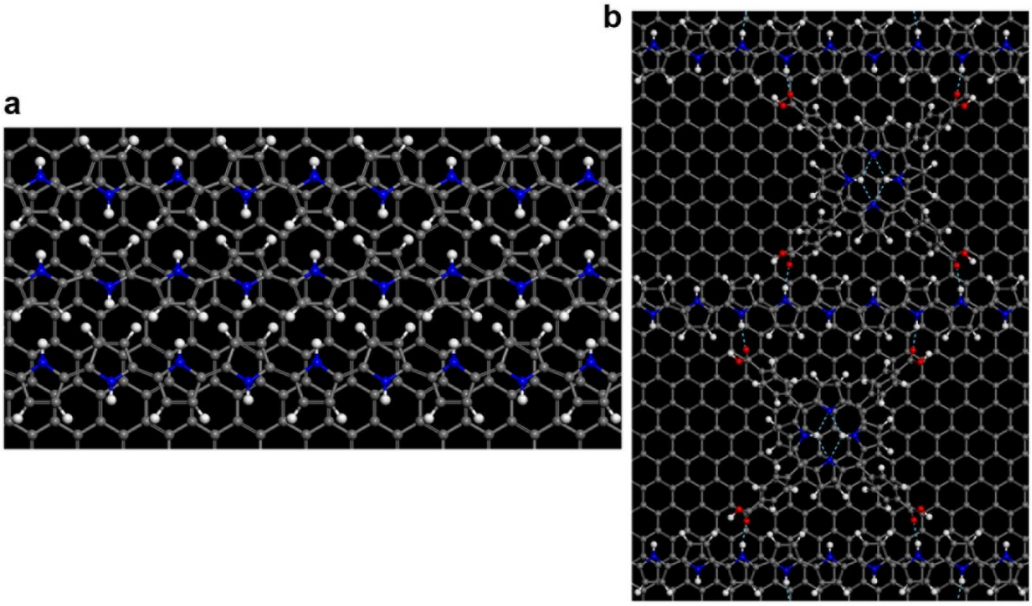

Figure S18. DFT optimized geometries of PPy on carbon mono layer (a) and PPy on carbon mono layer doped by TCPP cross-linker (b)

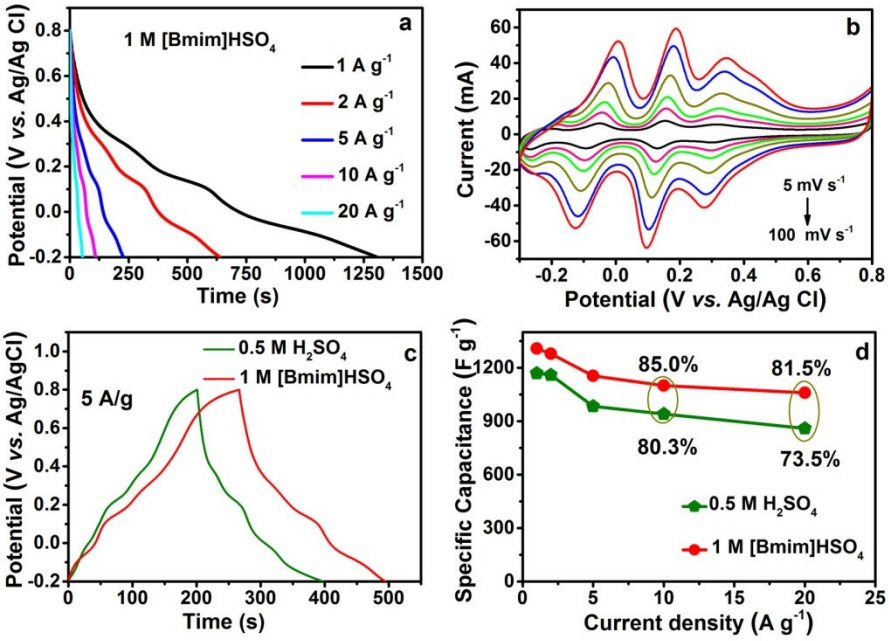

Figure S19. GCD branch (a) and CV curves (b) of PMo_{12}/PPy/CNT hydrogel electrode in 1 M [Bmim]HSO_4 aqueous solutions; (c) GCD curves of PMo_{12}/PPy/CNT hydrogel electrode in 0.5 M H_2SO_4 and 1 M [Bmim]HSO_4 at 5A g^{-1}; (d) Specific capacitances of PMo_{12}/PPy/CNT hydrogel electrode in different electrolytes at various current densities

Table S2. Comparison of specific capacitance of PMo_{12}/PPy/CNT hybrid hydrogel with other reported POMs-based composite materials

Materials	Electrolyte	Current density/Scan rate	Specific capacitance	Ref.
PMo_{12}/PPy/CNT gel	0.5 M H_2SO_4	1 A g^{-1}	1170 F g^{-1}	Ours
PMo_{12}/PPy/CNT gel	1 M [Bmim]HSO_4	1 A g^{-1}	1308 F g^{-1}	Ours
MoS/rGO	0.5MNa_2SO_4+H_2SO_4	10 mV s^{-1}	870 F g^{-1}	5
NENU-5/PPy-0.15	3M KCl	10 mV/s	779.8 F g^{-1}	6
CDs-PMo_{12}-PANI	1 M H_2SO_4	1 A g^{-1}	479 F g^{-1}	7
PMo_{12}/PANI/TiN NWA	1 M H_2SO_4	1 A g^{-1}	469 F g^{-1}	8
SWCNT-TBA-PV_2Mo_{10}	1 M H_2SO_4	10 mV s^{-1}	444 F g^{-1}	9
PIL/POM/RGO	0.5 M H_2SO_4	1 A g^{-1}	443 F g^{-1}	10
MXene-PIL-POM	0.5 M H_2SO_4	1 A g^{-1}	384.6 F g^{-1}	11
Pinecone AC/PMo_{12}	1 M H_2SO_4	10 mV s^{-1}	361 F g^{-1}	12
PPy-PMo_{12}/rGO	0.5 M H_2SO_4	1 A g^{-1}	295 F g^{-1}	2
Cs-PMo_{12}/CNT	Nafion+1 M H_2SO_4	0.2 A g^{-1}	285 F g^{-1}	13
PMo_{12}-PANI	---	20 mV/s	363.5 F g^{-1}	14
PMo_{12}@PPy	1 M H_2SO_4	2 mA/cm2	294.1 F g^{-1}	15
AC@PMo_{12}	1 M[Bmim]HSO_4	1 mV/s	223 F g^{-1}	16
PMo_{12}/PANI	---	1 A g^{-1}	376	17
$(GO/PMo)_{20,96}$	0.5 M H_2SO_4	10 mV/s	207 F g^{-1}	18
$GeMo_{12}$-$SiMo_{12}$-MWCNT	1 M H_2SO_4	100 mV s^{-1}	191.2 F cm^{-3}	19
PAni-0.5%PMo_{12}	1 M H_2SO_4	1 mA cm^{-2}	172.38 F g-1	20
rGO-PMo_{12}	1 M H_2SO_4	5 A g^{-1}	299 F g^{-1}	21
RGO/PMo_{12}	1 M H_2SO_4	10 mV s^{-1}	276 F g^{-1}	22
AC/$PW_{12}O_{40}$	1 M H_2SO_4	10 mV s^{-1}	254 F g^{-1}	23
HPW/RGO	5 M H_2SO_4	1 A g^{-1}	154.4 F g^{-1}	24
$[Ag_5(brtmb)_4][VW_{10}V_2O_{40}]$	1 M H_2SO_4	110 A g^{-1}	206 F g^{-1}	25
$Na_6V_{10}O_{28}$	1m $LiClO_4$	0.1 A g-1	354 F g^{-1}	26
AC/P_2Mo_{18}	1 M H_2SO_4	6 A g^{-1}	275 F g^{-1}	27
PMoW-PDDA-RGO	1 M H_2SO_4	1 A g^{-1}	279.1 F g^{-1}	28
$(H_2bpe)(Hbpe)_2\{[Cu(pzta)(H_2O)][P_2W_{18}O_{62}]\}.5H_2O$	1 M H_2SO_4	5 A g^{-1}	168 F g^{-1}	29
$[Ru(bpy)_3]_3PMo_{18}O_{62}$. nH_2O	-	0.2 A g^{-1}	68 F g^{-1}	30
$[Ru(bpy)_3]_{3.33}PMo_{18}O_{62}mH_2O$	0.25 M total salt	0.2 A g^{-1}	125 F g^{-1}	30
$[PW_{11}CoO_{39}]_5$-@Ru-rGO	0.5 M HOAC	0.2 A g^{-1}	624 F g^{-1}	31
$[PW_{11}NiO_{39}]_5$-@Ru-rGO	0.5 M HOAC	0.2 A g^{-1}	568 F g^{-1}	31
$[PW_{11}CuO_{39}]_5$-@Ru-rGO	0.5 M HOAC	0.2 A g^{-1}	705 F g^{-1}	31
AC/PMo_{12}	1 M H_2SO_4	2 A g^{-1}	160 /183 F g^{-1}	32
$\{Ag_5(pz)_7\}(BW_{12}O_{40})$	1 M H_2SO_4	2.16 A g^{-1}	1058 F g^{-1}	33
$\{Ag_5(pz)_7\}(SiW_{12}O_{40})](OH)\cdot H_2O$	1 M H_2SO_4	2.16 A g^{-1}	986 F g^{-1}	33
(Hpyr)[$\{Ag(pz)\}_2(PMo_{12}O_{40})$	1 M H_2SO_4	2.16 A g^{-1}	1611 F g^{-1}	33
POM-Ppy/nanopillar	0.05 M H_2SO_4	1mA cm^{-2}	77.0 mF cm^{-2}	34
$\{Mo_{132}\}$-rGO	1 M Li_2SO4	5A g^{-1}	617.3 F g^{-1}	35
HT-RGO-PMo_{12}	1 M H_2SO_4	10 mV s^{-1}	276 F g^{-1}	36
Mo_{132}-DTAB-EEG	1 M H_2SO_4	1 mV s^{-1}	65 F g^{-1}	37
GO/PMo_{12}	1 M H_2SO_4	10 mV s^{-1}	207 F g^{-1}	38
Co-POM/rGO	1 M H2SO4	0.5A g^{-1}	211.3 F g^{-1}	39

Table S3. Comparison of specific capacitance of PPy/PMo_{12}/CNT ternary hybrid hydrogel-based liquid-state supercapacitor (LSC) with other reported LSCs made of POMs-based composites electrodes

Materials	Device	Electrolyte	Current density /Scan rate	Specific capacitance	Ref.
PMo_{12}/PPy/CNT gel	Symmetric	1 M [Bmim]HSO_4	1 mA cm^{-2}	577.74 mF cm^{-2}	Ours
PMo_{12}/PPy/CNT gel	Symmetric	1 M [Bmim]HSO_4	10 mV s^{-1}	272.0 F g^{-1}	Ours
PMo_{12}@PPy	Symmetric	1 M H_2SO_4	5 mA cm^{-2}	71.6 mF cm^{-2}	15
SWCNT-TBA-PV_2Mo_{10}	Symmetric	1 M H_2SO_4	1 mA cm^{-2}	224 mF cm^{-2}	9
PMo_{12}/MWCNT	Symmetric	1 M H_2SO_4	1 A g^{-1}	40 F g^{-1}	40
PMo_{12}/PPy//PW_{12}/PEDOT	Asymmetric	0.5 M H_2SO_4	1 mA g^{-1}	31 F g^{-1}	41
PMo_{12}/PAni	Symmetric	0.5 M H_2SO_4	0.05 mA cm^{-2}	195 mF cm^{-2}	42
rGO-PMo_{12}//rGO-PW_{12}	Asymmetric	1 M H_2SO_4	2 mA cm^{-2}	110.9 F g^{-1}	21
PIL/POM/RGO	Symmetric	0.5 M H_2SO_4	0.5 A g^{-1}	408 F g^{-1}	10
{Mo_{132}}-rGO	Asymmetric	1 M $LiSO_4$	0.2 A g^{-1}	52.7 F g^{-1}	35
AC/PMo_{12}	Symmetric	1 M H_2SO_4	1A g^{-1}	45 F g^{-1}	32
HT-RGO-PMo_{12}	Symmetric	1 M H_2SO_4	1A g^{-1}	123 F g^{-1}	36
PMoW-PDDA-RGO	Symmetric	1M H_2SO_4	1A g^{-1}	177 F g-1	28
Cs-PMo_{12}/CNT	Symmetric	1 M H_2SO_4	1 A g^{-1}	30 F g^{-1}	13

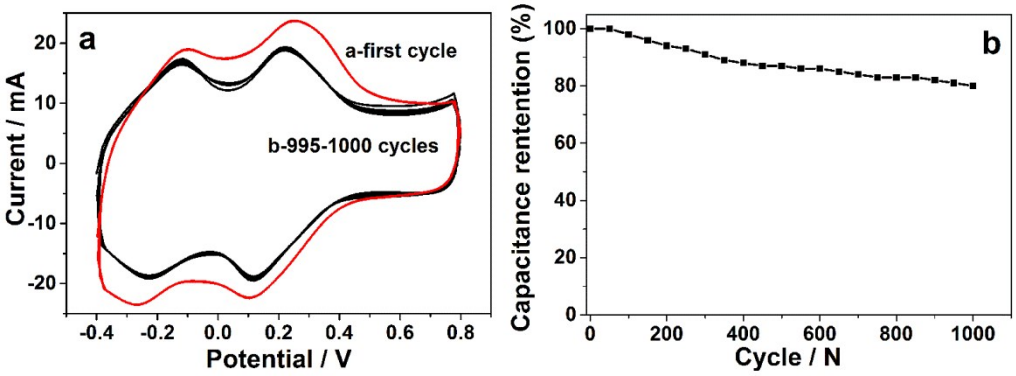

Figure S20. 1000 cycles continuous CV tests of PMo_{12}/PPy/CNT gel-based LSC (a) and corresponding cycle life

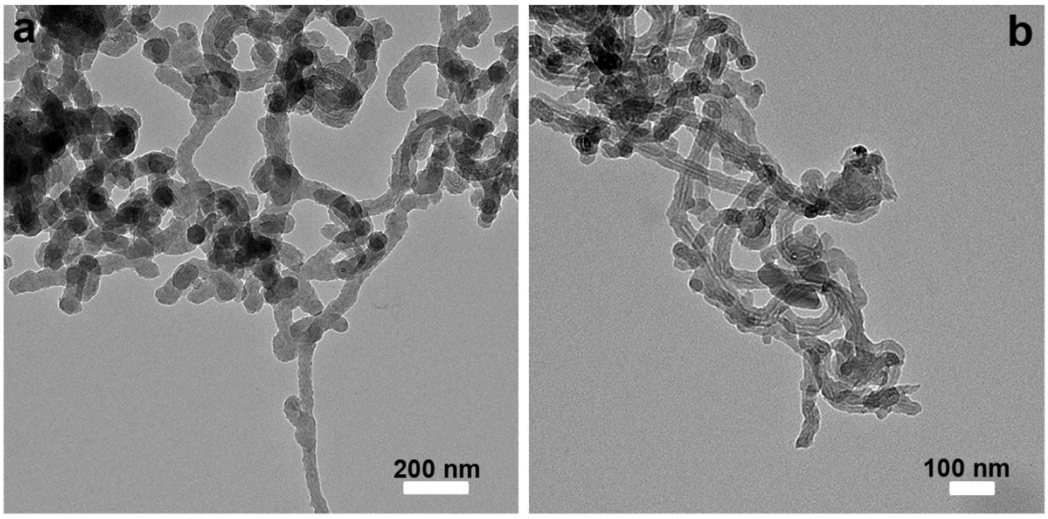

Figure S21. HRTEM images of PMo_{12}/PPy/CNT hybrid hydrogel before and after 605 CV cycles

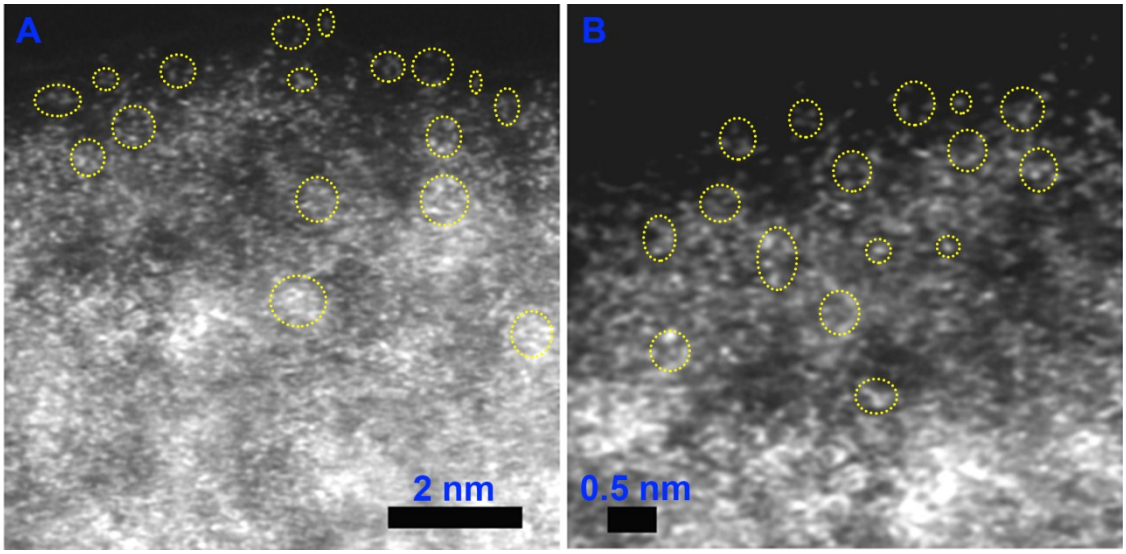

Figure S22. HADDF-STEM images of PMo_{12}/PPy/CNT hybrid hydrogel before and after 605 CV cycles

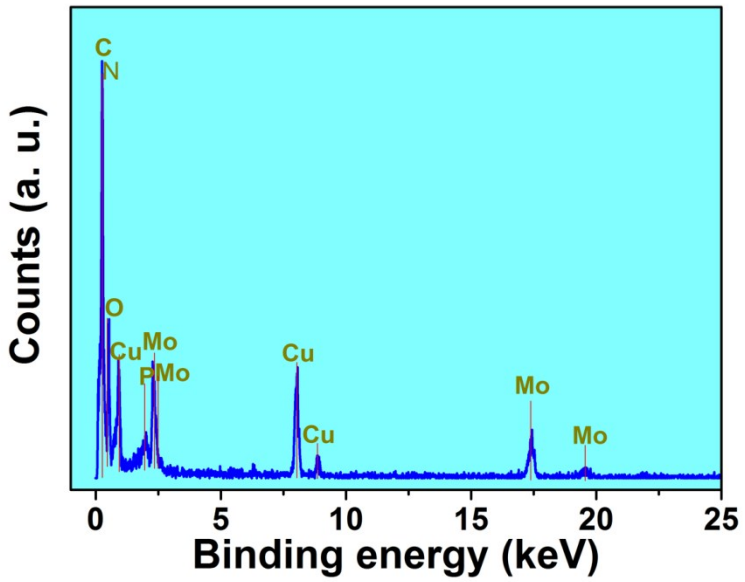

Figure S23. Energy dispersive X-ray spectrometry (EDX) spectrum of PMo_{12}/PPy/CNT hybrid hydrogel after 605 CV cycles

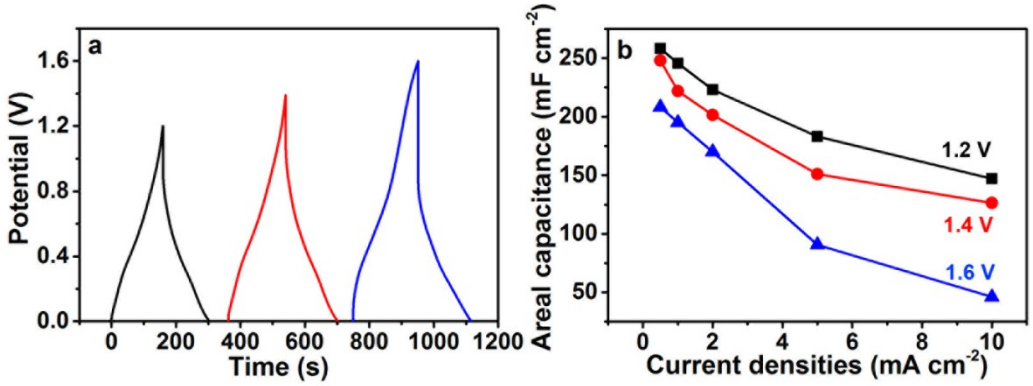

Figure S24. GCD cycles for PMo_{12}/PPy/CNT hydrogel-based SSC in the voltage windows of 0-1.2 V, 0-1.4 V and 0-1.6 V at current density of 1.0 mA cm^{-2} (a); Specific capacitances of SSCs in different voltage windows at various current densities (b)

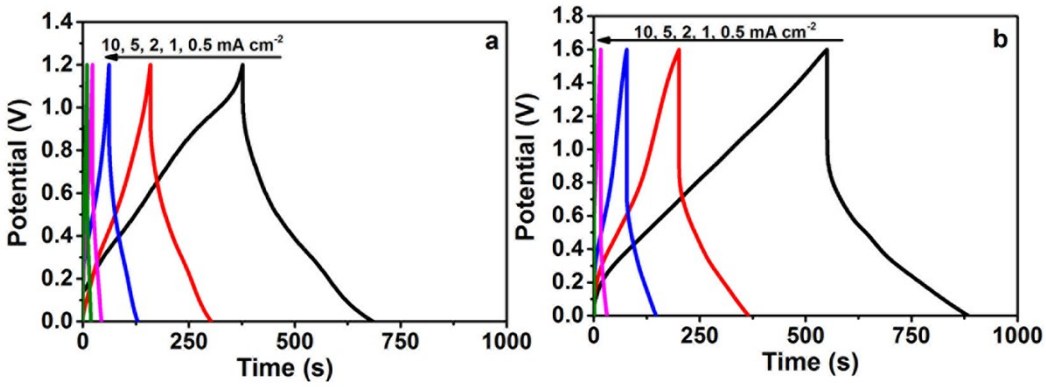

Figure 25. GCD cycles for PMo_{12}/PPy/CNT hydrogel-based SSC in the voltage windows of 0-1.2 V and 0-1.6 V

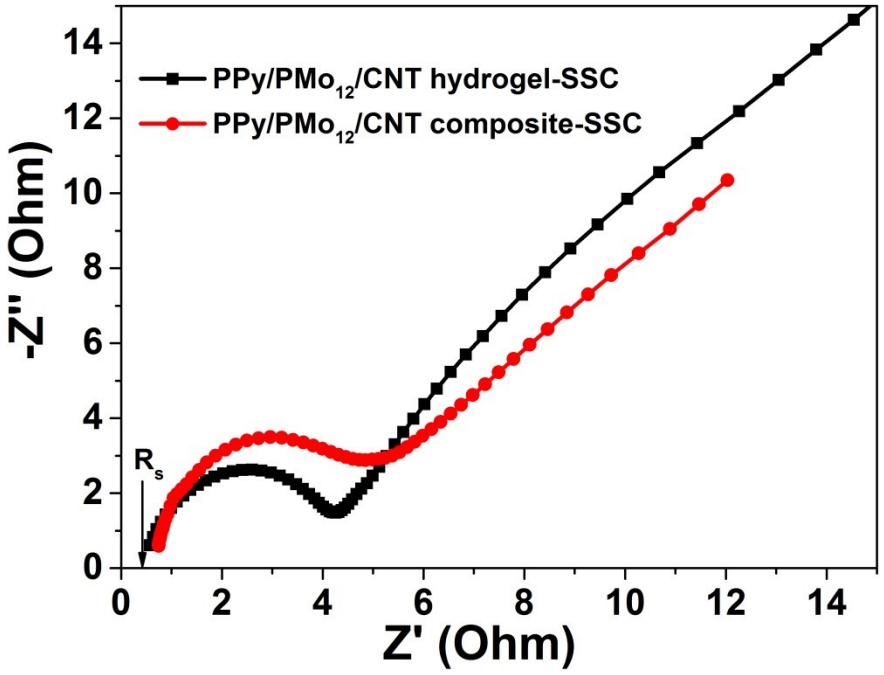

Figure S26. Nyquist plots of two-electrode solid device based on PPy/PMo_{12}/CNT ternary hybrid hydrogel and conventional PPy/PMo_{12}/CNT composite

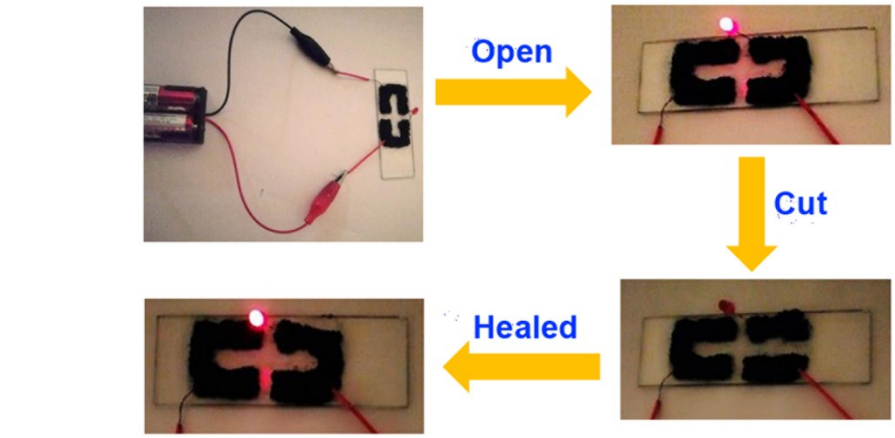

Figure S27. Pictures showing that the PPy hydrogel is conductive and flexible

The high conductivity and flexibility of PMo_{12}/PPy/CNT gel were also studied by designing a complete circuit including an LED bulb, in which PMo_{12}/PPy/CNT gel as the conductor and two dry batteries (1.5 V) as the power source. The bulb was successfully lighted when the circuit was switched to close status, indicating the high conductivity of our hybrid gel. In the test, the right side of PMo_{12}/PPy/CNT hybrid gel was cut and the circuit then became open and the bulb was extinguished. After that the circuit was re-established, and the LED bulb could be lighted up again, showing good conductivity of PMo_{12}/PPy/CNT hybrid gel. In addition, the hybrid hydrogel can self-heal after being cut off.

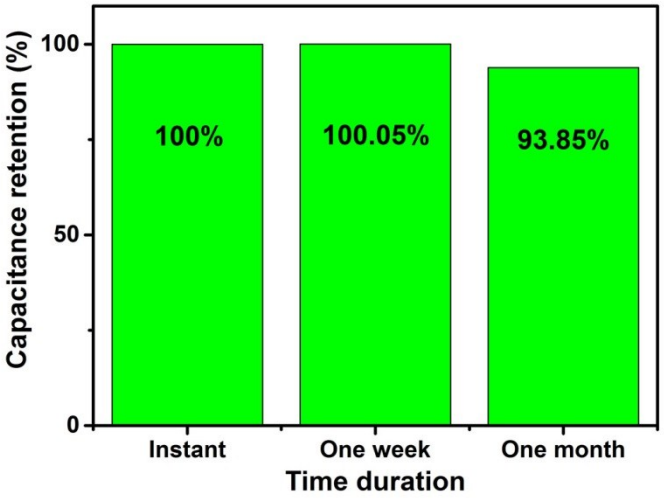

Figure S28. Capacitance retention calculated form GCD curves at 1 mA cm^{-2} of a SSC device at the bending angle of 120° after different time durations

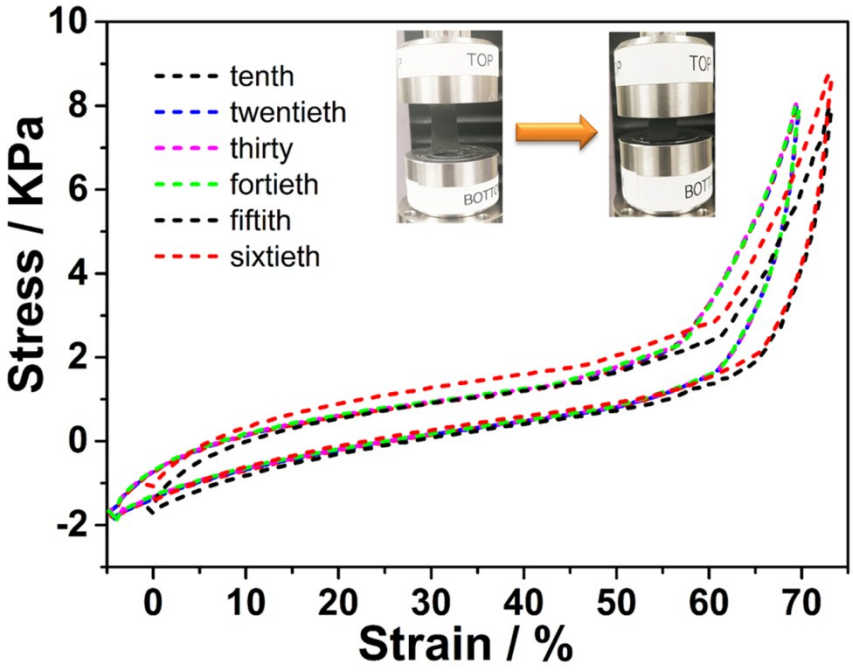

Figure S29. Compression cycles of the flexible solid-state supercapacitor

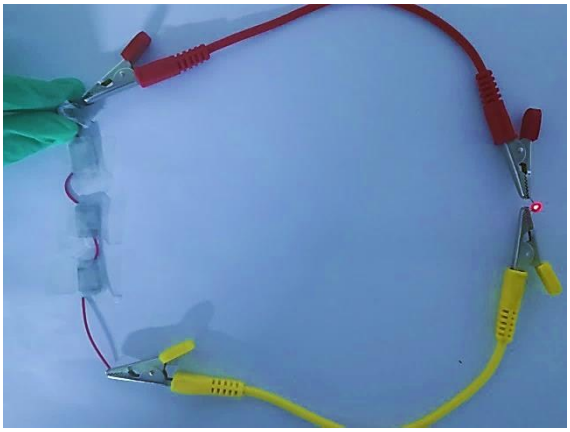

Figure S30. A red LED powered by four capacitors connected in series, in which one is in bending state

Reference

[1] D. Dubal, B. Ballesteros, A. Mohite, P. Gomezromero, Functionalization of polypyrrole nano-pipes with redox-active polyoxometalates (POMs) for ultrahigh energy density supercapacitors, Chemsuschem, 10 (2017) 731.

[2] C. Yuyun, H. Min, T. Yujia, B. Jianchun, L. Shunli, L. Yaqian, D. Zhihui, Polypyrrole-polyoxometalate/reduced graphene oxide ternary nanohybrids for flexible, all-solid-state supercapacitors, Chemical Communications, 51 (2015) 12377-12380.

[3] D. Hulicova, J. Yamashita, Y. Soneda, A. Hiroaki Hatori, M. Kodama, Supercapacitors prepared from melamine-based carbon, Chemistry of Materials, 17 (2005) 1241-1247.

[4] J.W. To, Z. Chen, H. Yao, J. He, K. Kim, H.H. Chou, L. Pan, J. Wilcox, Y. Cui, Z. Bao, Ultrahigh surface area three-dimensional porous graphitic carbon from

conjugated polymeric molecular framework, Acs Central Science, 1 (2015) 68-76.

[5] R.L. Shuangshuang Zhang, Shiwen Li, Anne Dolbecq, Pierre Mialane, Lin Suo, Lihua Bi, Baofang Zhang,Tianbo Liu,Caixia Wu, Likai Yan, Zhongmin Su, Guangjin Zhang, BinetaKeitah, Simple and efficient polyoxomolybdate-mediated synthesis of novel graphene and metal nanohybrids for versatile applications, Journal of Colloid and Interface Science, 514 (2018) 507-516.

[6] H.N. Wang, M. Zhang, A.M. Zhang, F.C. Shen, X.K. Wang, S.N. Sun, Y.J. Chen, Y.Q. Lan, Polyoxometalate-based metal-organic frameworks with conductive polypyrrole for supercapacitors, ACS Appl. Mater. Interfaces, 10 (2018) 32265-32270.

[7] L. Lu, Y.B. Xie, Phosphomolybdic acid cluster bridging carbon dots and polyaniline nanofibers for effective electrochemical energy storage, Journal of Materials Science, 54 (2019) 4842-4858.

[8] L. Lu, Y.B. Xie, Fabrication and supercapacitor behavior of phosphomolybdic acid/polyaniline/titanium nitride core-shell nanowire array, New J. Chem., 41 (2017) 335-346.

[9] H.Y. Chen, R. Al-Oweini, J. Friedl, C.Y. Lee, L. Li, U. Kortz, U. Stimming, M. Srinivasan, A novel SWCNT-polyoxometalate nanohybrid material as an electrode for electrochemical supercapacitors, Nanoscale, 7 (2015) 7934-7941.

[10] M.H. Yang, B.G. Choi, S.C. Jung, Y.y. Han, B.L. Sang, Polyoxometalate-coupled graphene via polymeric ionic liquid linker for supercapacitors, Advanced Functional Materials, 24 (2015) 7301-7309.

[11] S. Chen, Y. Xiang, M.K. Banks, C. Peng, W. Xu, R. Wu, Polyoxometalate-

coupled MXene nanohybrid via poly(ionic liquid) linkers and its electrode for enhanced supercapacitive performance, Nanoscale, (2018).

[12] M. Genovese, K. Lian, Polyoxometalate modified pine cone biochar carbon for supercapacitor electrodes, Journal of Materials Chemistry A, 5 (2017).

[13] A. Cuentas-Gallegos, R. Martinez-Rosales, M. Baibarac, P. Gomez-Romero, M.E. Rincon, Electrochemical supercapacitors based on novel hybrid materials made of carbon nanotubes and polyoxometalates, Electrochem. Commun., 9 (2007) 2088-2092.

[14] Z.M. Cui, C.X. Guo, W.Y. Yuan, C.M. Li, In situ synthesized heteropoly acid/polyaniline/graphene nanocomposites to simultaneously boost both double layer- and pseudo-capacitance for supercapacitors, Physical Chemistry Chemical Physics, 14 (2012) 12823-12828.

[15] D.P. Dubal, B. Ballesteros, A.A. Mohite, P. Gómez-Romero, Functionalization of polypyrrole nanopipes with redox-active polyoxometalates for high energy density supercapacitors, Chemsuschem, 10 (2017) 731.

[16] C. Hu, E. Zhao, N. Nitta, A. Magasinski, G. Berdichevsky, G. Yushin, Aqueous solutions of acidic ionic liquids for enhanced stability of polyoxometalate-carbon supercapacitor electrodes, J. Power Sources, 326 (2016) 569-574.

[17] C. Zhiming, G. Chun Xian, Y. Weiyong, L.C. Ming, In situ synthesized heteropoly acid/polyaniline/graphene nanocomposites to simultaneously boost both double layer- and pseudo-capacitance for supercapacitors, Physical Chemistry Chemical Physics, 14 (2012) 12823-12828.

[18] J.P. Wang, X. Wang, D.W. Gu, C.H. Liu, L.J. Shen, Synthesis and characterization of polyoxometalate/graphene oxide nanocomposites for supercapacitor, Ceram. Int., 44 (2018) 17492-17498.

[19] M. Genovese, K. Lian, Ionic Liquid-derived Imidazolium cation linkers for the layer-by-layer assembly of polyoxometalate-MWCNT composite electrodes with high power capability, ACS Appl Mater Interfaces, 8 (2016) 19100-19109.

[20] A. Manivel, A.M. Asiri, K.A. Alamry, T. Lana-Villarreal, S. Anandan, Interfacially synthesized PAni-PMo_{12} hybrid material for supercapacitor applications, Bull. Mat. Sci., 37 (2014) 861-869.

[21] D.P. Dubal, N.R. Chodankar, A. Vinu, D.H. Kim, P. Gomez-Romero, Asymmetric supercapacitors based on reduced graphene oxide with different polyoxometalates as positive and negative electrodes, Chemsuschem, 10 (2017) 2742-2750.

[22] J. Suarez-Guevara, V. Ruiz, P. Gomez-Romero, Stable graphene-polyoxometalate nanomaterials for application in hybrid supercapacitors, Physical Chemistry Chemical Physics, 16 (2014) 20411-20414.

[23] J. Suarez-Guevara, V. Ruiz, P. Gomez-Romero, Hybrid energy storage: high voltage aqueous supercapacitors based on activated carbon-phosphotungstate hybrid materials, J. Mater. Chem. A, 2 (2014) 1014-1021.

[24] R. Li, C.G. He, L. Cheng, G.Y. Lin, G.C. Wang, D. Slit, R.K.Y. Li, Y.K. Yang, Polyoxometalate-enabled photoreduction of graphene oxide to bioinspired nacre-like composite films for supercapacitor electrodes, Compos. Pt. B-Eng., 121 (2017) 75-82.

[25] G. Wang, T. Chen, X. Wang, H. Ma, H. Pang, G. Wang, T. Chen, X. Wang, H. Ma, H. Pang, A high-performance supercapacitor afforded by a high-connected keggin based 3D coordination polymer, European Journal of Inorganic Chemistry, 2017 (2017).

[26] H.Y. Chen, G. Wee, R. Al-Oweini, J. Friedl, K.S. Tan, Y. Wang, C.L. Wong, U. Kortz, U. Stimming, M. Srinivasan, A polyoxovanadate as an advanced electrode material for supercapacitors, Chemphyschem, 15 (2014) 2162-2169.

[27] A. Mu, J. Li, W. Chen, X. Sang, Z.M. Su, E. Wang, The composite material based on Dawson-type polyoxometalate and activated carbon as the supercapacitor electrode, Inorganic Chemistry Communications, 55 (2015) 149-152.

[28] Y.H. Ding, J. Peng, H.Y. Lu, Y. Yuan, S.U. Khan, Tungsten addenda mixed heteropolymolybdates supported on functionalized graphene for high-performance aqueous supercapacitors, Rsc Advances, 6 (2016).

[29] G. Wang, T. Chen, S. Li, H. Pang, H. Ma, A coordination polymer based on dinuclear (pyrazinyl tetrazolate) copper(ii) cations and Wells-Dawson anions for high-performance supercapacitor electrodes, Dalton Trans, 46 (2017) 10.1039.C1037DT02230A.

[30] S. Chinnathambi, M. Ammam, A molecular hybrid polyoxometalate-organometallic moieties and its relevance to supercapacitors in physiological electrolytes, Journal of Power Sources, 284 (2015) 524-535.

[31] A.A. Ensafi, E. Heydarisoureshjani, B. Rezaei, $[PW_{11}MO_{39}]^{5-}$ decorated on Ru-reduced graphene oxide nanosheets, characterizations and application as a high

performance storage energy and oxygen reduction reaction, Chemical Engineering Journal, (2017) S1385894717314031.

[32] V. Ruiz, J. suárze-Guevara, P. Gomez-Romero, Hybrid electrodes based on polyoxometalate—carbon materials for electrochemical supercapacitors, Electrochemistry Communications, 24 (2012) 35-38.

[33] L.G. Nana Du, Lingyu Fan, Kai Yu, Huan Luo, Shengjie Pang, Jiaqian Gao, Zhuwu Zheng, Jinghua Lv, and Baibin Zhou, Nanocomposites Containing keggin anions anchored on pyrazine based frameworks for use as supercapacitors and photocatalysts, ACS Applied Nano Materials, DOI: 10.1021/acsanm.9b00409 (2019).

[34] M. Yang, S.B. Hong, J.H. Yoon, D.S. Kim, S.W. Jeong, D.E. Yoo, T.J. Lee, K.G. Lee, S.J. Lee, B.G. Choi, Fabrication of flexible, redoxable, and conductive nanopillar arrays with enhanced electrochemical performance, ACS Appl Mater Interfaces, 8 (2016) acsami.6b06579.

[35] L.C. Yina Dong, Weilin Chen, Xiaotao Zheng, Xinlong Wang, Enbo Wang, rGO functionalized with a highly electronegative Keplerate-Type polyoxometalate for high-energy-density aqueous asymmetric supercapacitors, Chemistry -An Asian Journal, 13 (2018) 3304-3313.

[36] J. Suárez-Guevara, V. Ruiz, P. Gómez-Romero, Stable graphene–polyoxometalate nanomaterials for application in hybrid supercapacitors, Physical Chemistry Chemical Physics, 16 (2014) 20411-20414.

[37] A.G. Dawid Pakulski, Włodzimierz Czepa,Zhaoyang Liu, Luca Ortolani, Vittorio Morandi, Violetta Patroniak, Artur Ciesielski, Paolo Samorì, Novel Keplerate type

polyoxometalate-surfactant-graphene hybrids as advanced electrode materials for supercapacitors, Energy Storage Materials, 17 (2019) 186-193.

[38] X.W. Jipeng Wang, Dawei Gu, Changhua Liu, Linjiang Shen, Synthesis and characterization of polyoxometalate/graphene oxide nanocomposites for supercapacitor, Ceramics International, 44 (2018) 17492-17498.

[39] D. L. X. Z. H. C. J. L. Y. L. B. C. F. Q. S. H. F. Zhang, A high performance solid‐state asymmetric supercapacitor based on Anderson‐type polyoxometalate‐doped graphene aerogel, Research on Chemical Intermediates, 45 (2019) 3237–3250.

[40] M. Skunik, M. Chojak, I.A. Rutkowska, P.J. Kulesza, Improved capacitance characteristics during electrochemical charging of carbon nanotubes modified with polyoxometallate monolayers, Electrochim. Acta, 53 (2008) 3862-3869.

[41] G.M. Suppes, C.G. Cameron, M.S. Freund, A Polypyrrole/phosphomolybdic acid vertical bar poly(3,4-ethylenedioxythiophene)/phosphotungstic acid asymmetric supercapacitor, J. Electrochem. Soc., 157 (2010) A1030-A1034.

[42] P. Gómez-Romero, M. Chojak, K. Cuentas-Gallegos, J.A. Asensio, P.J. Kulesza, N. Casañ-Pastor, M. Lira-Cantú, Hybrid organic–inorganic nanocomposite materials for application in solid state electrochemical supercapacitors, Electrochemistry Communications, 5 (2003) 149-153.

[43] J.Q. Qin, F. Zhou, H. Xiao, R. Ren, Z.S. Wu, Mesoporous polypyrrole-based graphene nanosheets anchoring redox polyoxometalate for all-solid-state micro-supercapacitors with enhanced volumetric capacitance, Sci. China-Mater., 61 (2018)

233-242.